Materials Today Bio 27 (2024) 101118

Contents lists available at ScienceDirect

Materials Today Bio

journal homepage: www.journals.elsevier.com/materials-today-bio

Advanced topology of triply periodic minimal surface structure for osteogenic improvement within orthopedic metallic screw

Wangwang Luo [a], Yang Wang [a], Zhonghan Wang [a,b], Jianhang Jiao [a], Tong Yu [a], Weibo Jiang [a], Mufeng Li [a], Han Zhang [a], Xuqiang Gong [c], Bo Chao [a], Shixian Liu [a], Xuhui Wu [a], Jincheng Wang [a,**], Minfei Wu [a,*,1]

[a] *Department of Orthopedics, The Second Hospital of Jilin University, Changchun, China*
[b] *Orthopaedic Research Institute of Jilin Province, Changchun, China*
[c] *Department of Spine Surgery, The First Affiliated Hospital of Harbin Medical University, Harbin, China*

ARTICLE INFO

Keywords:
Porous structure
Orthopedic implant
Bone
Regeneration

ABSTRACT

Metallic screws are one of the most common implants in orthopedics. However, the solid design of the screw has often resulted in stress shielding and postoperative loosening, substantially impacting its long-term fixation effect after surgery. Four additive manufacturing porous structures (Fischer-Koch S, Octet, Diamond, and Double Gyroid) are now introduced into the screw to fix those issues. Upon applying the four porous structures, elastic modulus in the screw decreased about 2~15 times to reduce the occurrence of stress shielding, and bone regeneration effect on the screw surface increased about 1~50 times to improve bone tissue regrowing. With more bone tissue regrowing on the inner surface of porous screw, a stiffer integration between screw and bone tissue will be achieved, which improves the long-term fixation of the screw tremendously. The biofunctions of the four topologies on osteogenesis have been fully explored, which provides an advanced topology optimization scheme for the screw utilized in orthopedic fixation.

1. Introduction

Metallic screws have wide range of clinical applications in orthopedics. They can be used alone in the internal fixation of fracture with different severity, such as avulsion fractures, transverse fractures, and oblique fractures [1–3]. They can also be applied as a fixation component for other orthopedic implants, for example the prostheses of interbody fusion cage and acetabular cup [4,5]. As a solid orthopedic implant manufactured with metal material, the overall elastic modulus of metallic screw is much greater than bone tissue [6,7]. Therefore, a phenomenon of uneven spatial distribution of internal elastic modulus will inevitably occur in the bone implanted with metallic screw. With the local high elastic modulus brought by the screw embedded, mechanical response of bone under stress condition would be changed subsequently. When external force is applied on the bone containing a metallic screw, stress will distribute more intensively in the screw compared to the vicinal bone tissue with low elastic modulus, which then causes the postoperative issue of stress shielding [8,9]. The occurrence of stress shielding can obviously reduce the mechanical stress of the normal bone tissue around the screw, and without sufficient mechanical stimulation, the normal bone tissue will degenerate gradually in the long term. Under weak mechanical stimulation, the processes of bone regeneration and maturation will be hindered, and the trabecular bone volume and thickness will slowly decrease [10,11]. Consequently, the mechanical strength of bone tissue could get damaged, and in the worst situation, deterioration of the bone tissue near the metallic screw could result in osteoporosis or even pathological fracture after surgery [12,13]. When the fixed fracture block or prosthesis is subjected to high stress or acute violence, accidental fracture would more easily take place in those loose bone trabeculae near the solid screw, which could cause the screw loosening unavoidably and lead to the failure of screw fixation. The issues mentioned above could collectively increase the instability of the implanted screw over time, raising concerns regarding the long-term fixation of the metallic screw applied in

---

* Corresponding author. Department of Orthopedics, The Second Hospital of Jilin University, 218 Ziqiang Street, Changchun, 130041, China.
** Corresponding author. Department of Orthopedics, The Second Hospital of Jilin University, 218 Ziqiang Street, Changchun, China.
E-mail addresses: jinchengwangjlu@163.com (J. Wang), wumf@jlu.edu.cn (M. Wu).

[1] Minfei Wu is the main corresponding author who will handle Correspondence at all stages of refereeing and publication, also post-publication.

https://doi.org/10.1016/j.mtbio.2024.101118
Received 5 March 2024; Received in revised form 2 June 2024; Accepted 8 June 2024

orthopedics. Therefore, a second surgery is usually needed in clinic to remove the metallic screw implanted, especially for the patients with the underlying disease of osteoporosis, while this second surgery increases patients' the medical expenses and surgical pains tremendously [14–16]. In the development of stress shielding, material of which the screw is composed plays a very important role. The possibility of stress shielding is closely related to the mechanical and chemical properties of screw material. Stiffer and more corrosion-resistant material usually shows the higher possibility of stress shielding, for example titanium material and its alloy [17,18].

In order to reduce the occurrence of stress shielding in the vicinity of the screw implanted, the most crucial method is to reduce screw elastic modulus near the value range of natural bone tissue (1.2–22.3 GPa) [19]. Four strategies have been commonly used in the past research: a) introduce the low elastic modulus material into the high elastic modulus material or replace the high elastic modulus material with the lower one [20,21]; b) introduce the porous structure to decrease elastic modulus [22,23]; c) select the biodegradable material to reduce the duration of implant existence in human body [24,25]; d) improve the implant bioactivity on bone regeneration so as to compensate for the negative effect brought by stress shielding [26,27]. Among these four strategies, the second strategy is simpler and more direct on the reduction of elastic modulus. Furthermore, porous structure design applied in the orthopedic implant has been proven efficacious in inducing bone tissue ingrowth into the implant [28–30]. Using a porous structure in the metallic screw allows for increased bone tissue infiltration, gradually improving screw fixation strength after implantation as more bone tissue integrates with the screw. Consequently, the likelihood of the fixed screw loosening and falling out unexpectedly after surgery diminishes progressively [31,32]. An overall porous design in this metallic screw is quite necessary to promote its long-term fixation effect, and the second surgery of screw removing would be avoided when the porous design got introduced in the metallic screw [33,34].

Additive manufacturing technology mainly focuses on the biofunction optimization of porous orthopedic implants. With the development of additive manufacturing technology, some relevant *in vitro* experiments have found that the different topology and architecture in the implant could provide the different extracellular microenvironments for the contacted cells. The different extracellular microenvironments could then hugely affect their cellular behaviors including cell adhesion, migration, proliferation, and differentiation [35–38]. Moreover, some *in vivo* experiments have proved that the extra topology and architecture design adopted in the porous orthopedic implant could affect the regeneration rate of the implant-contacted interface tissue [39–42]. Optimizing the topology and architecture design allows for modulating the tissue ingrowth capability of a porous implant, thereby aligning it with the specific tissue type targeted for healing. To improve the fixing efficacy of the porous metallic screw utilized in orthopedics, a refined topology design that promotes bone tissue regeneration should be attained. This entails incorporating specific structures adept at stimulating bone tissue regrowth, enhancing the long-term fixation effect of the metallic screw.

This study introduces four prevalent additive manufacturing porous structure designs: Fischer-Koch S, Octet, Diamond, and Double Gyroid, extensively applied to other orthopedic implants, including metallic screws [43–51]. Fischer-Koch S, Diamond, and Double Gyroid structures are the three typical ones in the triply periodic minimal surface (TPMS) topology category [47,51], and the Octet structure is the classic one in the archetype topology category [49]. These four kinds of structures (TPMS and archetype topologies) belong to the metamaterial category, whose mechanical properties are defined by the different artificial structures rather than their compositions [48,52–54]. These four structures are ideal designs with high tissue biomimetic degrees, especially compared with the natural trabecular bone structure [48,55–57]. Additionally, these four structures are based on parametric designing, indicating that the porosities of the orthopedic implants under these structures could be modulated accurately by adjusting their relevant geometric parameters. Therefore, the mechanical properties of the orthopedic implants could be easily tuned into the bone tissue value range. Due to the above advantages, these four structure designs could be suitable for the topological optimization of the metallic screw used in orthopedics. For examining the practical bioeffects of the four structures to screen out the most superior ones for bone regeneration, this study has designed and fabricated the different scaffolds under the four structures and has conducted *in vitro* and *in vivo* experiments with the four kinds of scaffolds, hoping to explore the potential biological properties of these structure designs more clearly.

2. Materials and methods

2.1. Model design and analysis

The objects (orthopedic implants or scaffolds) under the porous structures of Fischer-Koch S, Octet, Diamond, and Double Gyroid were constructed by their corresponding representative volume elements (RVEs) (Fig. 1A). Representative volume element (RVE), also called repeating unit cell, is a basic concept in the research of additive manufacturing. It is the smallest volume element divided from a continuous or periodic structure, whose material behavior is exactly representative of the RVEs-piled-up continuous or periodic porous bulk [58,59]. The spatial structures of the four kinds of RVEs were strictly defined by the geometric parameters of the structural mathematical functions or archetype topology design (Table 1). Fischer-Koch S, Diamond, and Double Gyroid structures belong to the TPMS category, whose RVE meshes were restricted by the listed implicit functions. Conversely, the Octet structure belongs to the archetype category, whose RVE mesh was restricted by the fixed octahedral structure. Different kinds of topologies will bring different kinds of pores and inner surfaces, which hugely affect the biological behaviors (adhesion, migration, proliferation, etc.) of the cells contacting and growing on these scaffolds [35–38]. The introduction of TPMS structure can bring a special zero curvature inner surface without any surface self-intersection, while the introduction of archetype topology can bring a triangular inner structure whose neighboring struts intersect at 45° regularly. These differences on porous structure could potentially affect the biological behaviors of bone cell, such as cell proliferation and differentiation. As concluded in the past study, titanium lattices with the porosity of 50–70 % were recommended for achieving comparable stiffness and compressive strength, thus we selected the value of 70 % in view of scaffold lightweight effect [60]. And besides, porous scaffold under the pore size of around 500 μm was proved beneficial for bone regeneration, thus we designed our scaffold basing on this finding [61]. As the four topologies in our study are parametric designs, the ratio of pore size/lattice size in the four structures correspond to the specific value of porosity. After determining the values of both pore size and porosity, lattice size can be calculated, whose value is around 1 mm. This study used the Mathematica software (Version 12.0) to generate the four RVE 3D models, which were scaled into the 1 × 1 × 1 mm cubes for the following *in vitro* and *in vivo* scaffold design. These four RVE models represented the essential unit cells to build up the more complex *in vitro* and *in vivo* scaffolds. The crucial geometric parameters of $C1$, $d/Ø$, $C2$, $C3$, and $C4$ were accurately set as 0.305, 0.269, 0.365, 1.000, and 2.104, respectively, to unify the four RVE model porosities, pore sizes, and their corresponding scaffolds into the values of 70 % and 550 μm (the values similar to trabecular bone tissue) [60]. $C1 \sim C4$ are critical constants in the equations of TPMS structures, whose values can directly control the porosities and pore sizes within the different scaffolds. d is the diameter of the Octet strut, and $Ø$ is the diameter of the inscribed sphere within the Octet strut. Through modifying these two parameters, porosity and pore size within Octet scaffold can be accurately controlled. In the equations of TPMS structures, (x, y, z) are all the points coordinated within the porous mesh, which are also corresponding to the solution

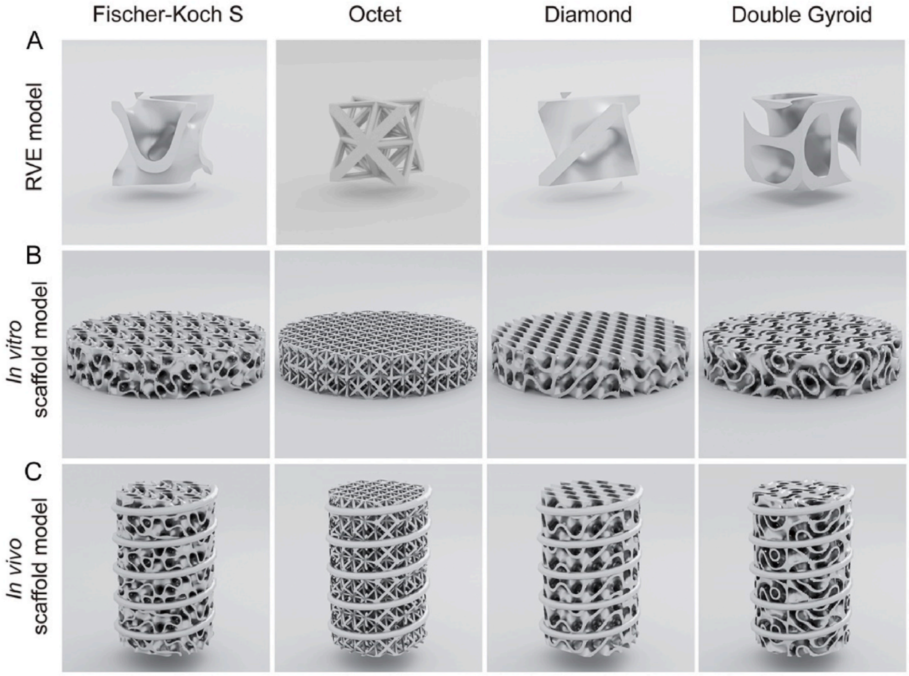

Fig. 1. **(A)** The RVE modes. **(B)** *In vitro* and **(C)** *in vivo* scaffold models of the four structures.

Table 1
The different RVE structures of Fischer-Koch S, Octet, Diamond and Double Gyroid.

Porous structure	RVE	Category	RVE Structure definition	Decisive parameters
Fischer-Koch S	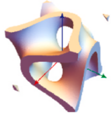	TPMS	Structural function	$F(x, y, z) = \mathrm{Cos}[\mathbf{2}x]\mathrm{Sin}[y]\mathrm{Cos}[z] + \mathrm{Cos}[\mathbf{2}y]\mathrm{Sin}[z]\mathrm{Cos}[x] + \mathrm{Cos}[\mathbf{2}z]\mathrm{Sin}[x]\mathrm{Cos}[y] \in [-\boldsymbol{C1}, \boldsymbol{C1}]$ [28,29]
Octet	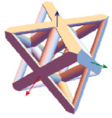	Archetype	Strut architecture of Octet archetype	$\boldsymbol{d/\O}$ [30]
Diamond	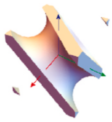	TPMS	Structural function	$F(x, y, z) = \mathrm{Sin}[x]\mathrm{Sin}[y]\mathrm{Sin}[z] + \mathrm{Sin}[x]\mathrm{Cos}[y]\mathrm{Cos}[z] + \mathrm{Cos}[x]\mathrm{Sin}[y]\mathrm{Cos}[z] + \mathrm{Cos}[x]\mathrm{Cos}[y]\mathrm{Sin}[z] \in [-\boldsymbol{C2}, \boldsymbol{C2}]$ [28,29]
Double Gyroid	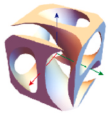	TPMS	Structural function	$F(x, y, z) = \mathbf{8}(\mathbf{1} - \boldsymbol{C3})\{\sin[\mathbf{2}x]\sin[z]\cos[y] + \sin[\mathbf{2}y]\sin[x]\cos[z] + \sin[\mathbf{2}z]\sin[y]\cos[x]\} - \mathbf{4}\boldsymbol{C3}\{\cos[\mathbf{2}x]\cos[\mathbf{2}y] + \cos[\mathbf{2}y]\cos[\mathbf{2}z] + \cos[\mathbf{2}z]\cos[\mathbf{2}x]\} \in [-\boldsymbol{C4}, \boldsymbol{C4}]$ [32]

x, y, z are the points coordinated within the mesh of Fischer-Koch S, Diamond, and Double Gyroid RVEs, which is also the solution set of the different functions assigned by any value within the corresponding value regions.
d is the diameter of the Octet strut, and ***Ø*** is the diameter of the inscribed sphere within the Octet strut.

sets when the equations are assigned by any value within the value regions. Following the four standard RVEs, the disc-shaped scaffold models with diameters of 10 mm and heights of 2 mm were designed for *in vitro* cytocompatibility experiments, and the cylindrical scaffold models with diameters of 5 mm and heights of 8 mm were designed for the *in vivo* experiments. For reducing the pressure concentration at screw thread, round cylindrical thread instead of sharp wedge thread was selected. The width and axial pitch of the screw thread in the *in vivo* scaffold model were set as 0.2 and 1.6 mm merged with the porous cylinder via Boolean calculation in Mathematica software (Fig. 1B and C). Since the nut structure in the conventional screw design does not bear stress after implantation, here we removed this nut structure for simplification [62–64]. The models were output in stereolithography (STL) file format, which was used for the following stress simulation analysis and 3D printing.

To analyze the mechanical properties of the four kinds of scaffolds before 3D printing, four simplified scaffold models composed of 2 × 2 × 2 different RVEs were constructed and input into the Comsol software (Version 5.3) for the stress analyses. In all the scaffold models, RVEs were composed according to the regular matrix arrangement, whose node spatial density is one per cubic millimeter. Due to the ideal mechanical strength and splendid biocompatibility among the common metals applied in orthopedic implants, the titanium alloy Ti6Al4V was selected as the mesh material for the scaffold analysis and 3D printing [65–67]. The mesh shapes and qualities of the four simplified scaffold models were set as "Tetrahedral" and "Subdivided" in the Comsol software (Fig. 2C). Subsequently, vertical boundary loads of 5×10^7 Pa were applied on their upper surfaces, fixed constraints were applied on their bottom surfaces, and eventually, the simulated von Mises stress distributions and elastic moduli could be calculated. In the next, torsional boundary loads of 5×10^3 N mm in the z-axis direction were applied in the similar way, and von Mises stress distributions of the four scaffolds under the torque force were emulated in Comsol software.

2.2. *Fabrication of the four topology-optimized in vitro and in vivo scaffolds*

Using the model STL files as input into the operating system, the *in*

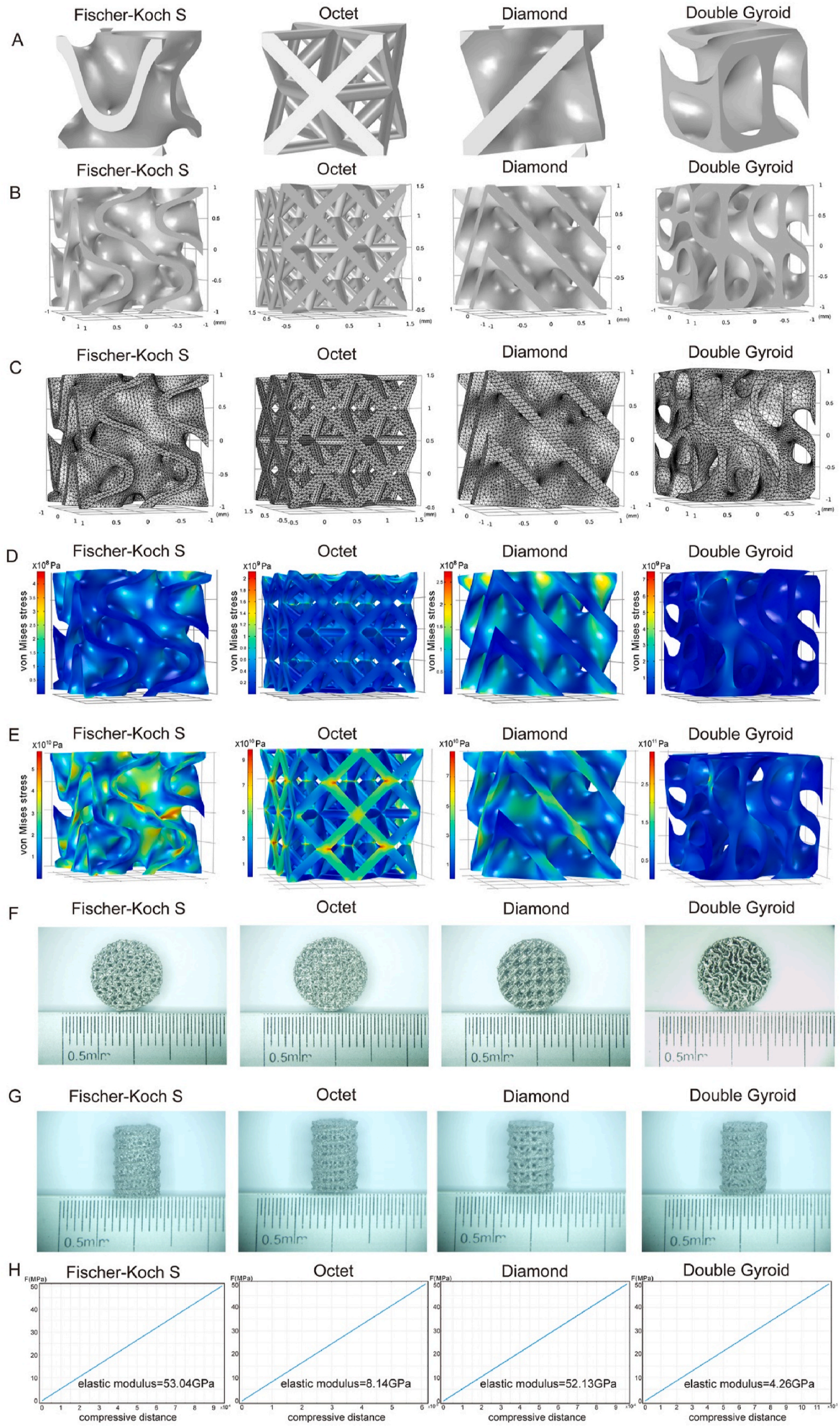

Fig. 2. **(A)** The different RVE modes, **(B)** 2 × 2 × 2 simplified scaffold models, **(C)** scaffold mesh subdivisions, **(D)** the von Mises stress distribution maps under compression forces, and **(E)** the von Mises stress distribution maps under torque forces. The printed **(F)** *in vitro* and **(G)** *in vivo* scaffolds of the four kinds of structures with an EBM 3D printer. **(H)** Elastic moduli of the four different scaffolds.

vitro and *in vivo* scaffolds were printed employing the EBM 3D printer (Arcam Q10 plus, Sweden). Ti6Al4V spherical powder (EOS GmbH, Krailling, Germany) with a diameter of 45–100 μm was selected for printing, and the residual powder inside these printed porous scaffolds was cleaned thoroughly via a quick wash with hydrofluoric acid (0.8 wt %) for 2 min and an overnight ultrasonic oscillation cleaning in water. The design and printing of the above scaffolds were completed at the Orthopedic Research Institute of Jilin Province, Changchun, China.

2.3. *Material and structure characterization*

The Ti6Al4V spherical powder sample and the four printed *in vitro* scaffolds were loaded into a scanning electron microscope (SEM; Regulus8100, HITACHI, Japan) equipped with an energy dispersive spectrometry (EDS; IXRF3310, IXRF Systems, America), whose surface morphologies and element compositions were analyzed in sequence.

2.4. *Mechanical test*

After screw being implanted into bone tissue, it could possibly endure many kinds of mechanical stresses, for example compression stress, tensile stress, and shear stress. Among these different stresses, compression stress along the direction of bone axis is more common. For exploring the actual mechanical property differences between the four structure designs, an electronic universal testing machine (ZWICK-Z250, ZwickRoell, Germany) was used to test the compression moduli and the yield strengths of the four structure-optimized *in vivo* scaffolds qualitatively. The compressing speed of the crosshead in the testing machine was set as 1 mm/min vertically, and the compressive stress-strain curves of the four kinds of scaffolds were output after the whole compression process.

2.5. *In vitro cell experiments*

2.5.1. *Cell culturing and seeding*

Mouse osteogenic precursor cells (MC3T3-E1; iCell M075™) were used to evaluate the osteogenic cytocompatibility and differentiation capacities of the four kinds of scaffolds. Resuscitated MC3T3-E1 cells were seeded in a Petri dish (100 × 20 mm) and subcultured until passage 3 into 10 mL of high-glucose Dulbecco's Modified Eagle Medium (DMEM) supplemented with 10 % fetal bovine serum, 1 % penicillin (100 U/mL), and streptomycin sulfate (100 mg/mL) (Gibco, Grand Island, NY). When the adherent cells covered about 90 % of the Petri dish, they were digested with 2 mL of trypsin (0.25 %) (Gibco, Grand Island, NY) for 2 min, centrifuged at 1200 rpm for 5 min, and resuspended with 5 mL of the corresponding culture medium. The cell resuspension concentration was calculated with a cell counting chamber and diluted into the same concentration of 2×10^5/mL with culture medium to prepare the standard cell suspensions for the following scaffold seeding. After the high-pressure steam sterilization, the four kinds of structure-optimized *in vitro* scaffolds were put into a 48-well plate. A standard cell suspension volume containing the corresponding cell number was added to the well and incubated for 2 h in the cell culture incubator (37 °C, 5 % CO_2, and saturated humidity) to perform the cell sedimentation and initial attachment onto the scaffolds. MC3T3-E1 cells grew on the different curved TPMS surfaces within Fischer-Koch S, Diamond, and Double Gyroid scaffolds or on the strut intersected surfaces within the Octet scaffold. For contrast, solid scaffold without any inner porous structure was set as the control group.

2.5.2. *Cell proliferation activities*

To detect MC3T3-E1 cell proliferation activities in the four kinds of scaffolds, Live/Dead cell staining (BestBio, BB-4126), cell counting Kit-8 assay (CCK-8; AbMole, M4839) and FITC-phalloidin/DAPI staining (Yeasen, 40735ES75) were performed in sequence. In Live/Dead cell staining experiments, 1×10^5 MC3T3-E1 cells were seeded on the four *in vitro* scaffolds and were cultured for 1, 3, and 5 days. The scaffolds at the different time points were stained by 400 μL of solution A (Calcein-AM; 1: 1000) for 30 min and then by 400 μL of solution B (PI; 1: 2000) for another 2 min. Solutions A and B were diluted with Hanks' Balanced Salt Solution (HBSS), and the staining was performed in the dark. The stained cells were gently washed twice with phosphate-buffered saline (PBS) and observed under an inverted microscope (Olympus Corporation, Japan). The CCK-8 assay was employed to evaluate the specific proliferation rates of the different cells in the four scaffolds. A total of 1×10^5 MC3T3-E1 cells were seeded on the four *in vitro* scaffolds, and the cell numbers in the scaffold at 1, 3, and 5 days of culturing were then analyzed with the CCK-8 assay. The scaffolds were soaked in 550 μL of HBSS-diluted CCK-8 solution and incubated for 2 h. The optical density (OD) values of the solutions were detected at the excitation wavelength of 450 nm, which represented the cell numbers at different time points, and standardized to evaluate the cell proliferation rates.

Besides the above two experiments detecting the influences of structure designs on cell proliferation, the FITC-phalloidin/DAPI staining experiment was conducted to determine the possible impact of the four structures on cellular morphology. Briefly, the samples collected on day three were pre-treated with 4 % paraformaldehyde and Triton X-100 solutions to fix the cells and increase their permeability. The treated samples were stained using FITC-phalloidin (1: 200 PBS) for the cytoskeletons and DAPI (1: 500 PBS) for the nuclei. The staining was conducted in darkness, and the stained samples were observed and imaged under an inverted microscope (Olympus Corporation, Japan).

2.5.3. *Alizarin Red S staining*

The Alizarin Red S staining experiment was performed with the four *in vitro* scaffolds to detect the possible influences on the extracellular calcium deposition caused by the different structure designs. One milliliter of standard MC3T3-E1 cell suspension (2×10^5 cells) was seeded on each scaffold, which was cultured with osteogenic medium (culture medium was supplemented with ascorbic acid (50 mg/L), disodium β-glycerophosphate (10 mmol/L) and dexamethasone (10^{-8} mol/L)) for 4, 7 and 14 days. The samples at the different time points were pre-treated with 4 % paraformaldehyde for cell fixation and were then stained with 500 μL of Alizarin Red S solution (Beyotime, C0138) for 30 min. The stained samples were gently washed twice with distilled water, dried in the air for 10 min, and observed and imaged under an ordinary optical microscope. To further quantify the exact content of extracellular calcium deposition in the different scaffolds, all the stained samples were soaked in 400 μL of cetylpyridinium chloride (CPC) solution (10 wt%) and incubated for 30 min. The OD values of CPC solutions were detected at the excitation wavelength of 562 nm, representing the quantities of extracellular calcium deposition produced by MC3T3-E1 cells at different time points.

2.5.4. *Alkaline phosphatase (ALP) test*

One milliliter of standard MC3T3-E1 cell suspension (2×10^5 cells) was seeded on each scaffold, which was then cultured with osteogenic medium for 7 and 14 days. At the corresponding time points, each sample was treated with 500 μL of RIPA Lysis Buffer (Beyotime, P0013K) to extract all the proteins of MC3T3-E1 cells growing in the four kinds of scaffolds. The total ALP activity (U) of each lysis solution was quantitatively analyzed with the ALP Assay Kit (Beyotime, P0321 M). A repeated seeding and culturing process was performed to eliminate the interference caused by different protein content. Two hundred microliters of RIPA lysis solution were used to extract all the proteins of MC3T3-E1 cells growing in the four kinds of scaffolds, and the total protein contents (mg) were then analyzed with the BCA Protein Assay Kit (Beyotime, P0012). The standardized ALP activities (U/mg) were calculated for the different samples by dividing the total ALP activity values by the total protein content values.

2.5.5. Reverse transcription-polymerase chain reaction (RT-PCR) assay

The osteogenesis-related gene expression of MC3T3-E1 cells were detected with RT-PCR techniques. One milliliter of standard MC3T3-E1 cell suspensions (2×10^5 cells) were seeded on the four kinds of scaffolds, which were cultured with osteogenic medium for 7 and 14 days, respectively. The total RNA of the different samples was extracted using a Total RNA Extraction Kit (Solarbio, R1200), and 1 μg of the extracted total RNA of each sample was used for cDNA synthesis. The synthesis was conducted using the SureScript First-Strand cDNA Synthesis Kit (GeneCopoeia, QP057). BlazeTaq SYBR GREE qPCR Mix (GeneCopoeia, QP033) was used as the mixed qPCR reagents to perform the following qPCR assays. β-actin was selected as the reference gene to normalize the osteogenesis-related gene expression level (ALP, OCN, OPN, Runx-2) in MC3T3-E1 cells. Table 2 lists all the primer sequences used, and all the gene expression results were calculated with the delta-delta Ct method ($2^{-\Delta\Delta Ct}$).

2.6. In vivo biocompatibility evaluation

To further evaluate the osteogenic capacities of the four kinds of scaffolds *in vivo*, adult male New Zealand white rabbits (3.0–3.5 kg) were used for the following surgeries and *in vivo* analyses. After being anesthetized with 10 % chlorpromazine hydrochloride (injected intramuscularly at 0.2 mL/kg), each rabbit underwent standard surgery to implant a specific scaffold into its distal femur. A bone defect with a radius of 5.5 mm and a depth of 10 mm was drilled at the medial condyle of the femur, and the specific *in vivo* scaffold was implanted into that defect, which would heal gradually in the next 6 or 12 weeks. All the surgeries were performed under sterile conditions, and the rabbits were treated with penicillin injection (10^5 U/d) for 3 days after the surgeries. After 6 or 12 weeks, the rabbits were euthanized to collect the distal femur samples, which were fixed with 4 % paraformaldehyde for the follow-up analyses. All relevant experimental procedures strictly followed the laws, regulations, and stipulations of animal ethics, which were approved by the Laboratory Teaching Center of Basic Medicine, Jilin University (approval number: No.2023430).

2.6.1. Micro-computed tomography (micro-CT) analysis

The collected distal femur samples were removed from the paraformaldehyde, dried in the air for 10 min, and scanned by micro-CT (Skyscan1076, Belgium) set as 70 kV voltage, 141 μA current, and 12.6 μm accuracy. The lower and upper observation grey thresholds were set as 40 and 255, respectively. Through the scanning processes, 3D reconstructions of the bone defects in the different samples were performed using CTVol (Version 2.0) software, which exhibited the 3D mapping of the new bone and implanted scaffolds within the corresponding defects. The data of those 3D reconstructions demonstrated several osteogenesis indices that were calculated quantitatively, including BV/TV (bone volume fraction: bone volume divided by the total volume of the defect), Tb. Th (trabecular thickness), Tb. Sp (trabecular separation), Tb. N (trabecular numbers), and BS/TV (bone surface area density: bone surface area divided by the total volume of the defect). These data were used to compare the new bone qualities in the different samples.

Table 2
The primer sequences of the genes that were detected in the RT-PCR test.

Gene	Forward primers	Reverse primers
β-actin	5′-AGGTCGGTGTGAACGGATTTG-3′	5′-TGTAGACCATGTAGTTGAGGTCA-3′
ALP	5′-AACCCAGACACAAGCATTCC-3′	5′-GAGAGCGAAGGGTCAGTCAG-3′
OCN	5′-AAGCAGGAGGGCAATAAGGT-3′	5′-TTTGTAGGCGGTCTTCAAGC-3′
OPN	5′-AGCAAGAAACTCTTCCAAGCAA-3′	5′-GTGAGATTCGTCAGATTCATCCG-3′
Runx-2	5′-ACTCTTCTGGAGCCGTTTATG-3′	5′-GTGAATCTGGCCATGTTTGTG-3′

2.6.2. Tissue section analysis

The fixed distal femur specimens were removed from the paraformaldehyde, dehydrated in 100 % acetone, and embedded in polymethyl methacrylate. The embedded tissues were cut into 300-μm-thick tissue sections (cut in the coronal plane of distal femurs to show the implanted scaffolds and defects longitudinally) using the hard tissue slicer (EXAKT300CP, German). The tissue sections were stained with hematoxylin, eosin, and toluidine blue. The stained sections were then observed and imaged under confocal microscopy (LEICA TCS SPE, German). The full-view images (5×), low-magnification images (12.5×), and high-magnification images (25 ×) of the sections were acquired, which showed the regenerated bone tissues within the defects and scaffolds in detail.

2.7. Statistical analysis

Data analysis was performed with the statistical software of GraphPad Prism (Version 9.2). All quantitative data are expressed as mean value ± standard deviation (SD). Three duplicate samples were set for each experimental group. Data were analyzed using the independent sample *t*-test and two-way analysis of variance (ANOVA). $p < 0.05$ indicated a statistically significant difference.

3. Results

3.1. Emulated stress distribution and scaffold fabrication

Fig. 2A and B shows the different RVE models and the 2 × 2 × 2 simplified scaffold models of the four structures in the Comsol software. The von Mises stress distribution maps of the simplified scaffold models, as calculated for their respective mesh subdivisions (Fig. 2C–E), illustrated that the significant stresses were uniformly distributed among the four porous structures. Scaffolds under those four porous structure designs were resistant to significant compressional and torsional stresses, which proved the ideal mechanical strengths of the four structures successfully. Fig. 2F and G presents the *in vitro* and *in vivo* scaffolds, which successfully proved the ideal printing effect of this EBM 3D printer. Elastic moduli of the four structures were calculated in Fig. 2H. In comparison to the elastic modulus of Ti6Al4V (110Gpa) [6,18], obvious reduction of elastic moduli could be achieved after these four porous structures being introduced into a solid Ti6Al4V implant.

3.2. Material and structure characterization and mechanical test

Fig. 3A and B represent the SEM and EDS images of the Ti6Al4V spherical powder sample and the four printed *in vitro* scaffolds. The four structures were entirely constructed using EBM 3D printing, resulting in the preservation of the primary element compositions and typical micro-topologies of these scaffolds. This confirmed the superior accuracy and stability of the EBM printing technique. The surface roughness of the four scaffolds was similar, guaranteeing that the possible biofunction differences of the four scaffolds would mainly result from their different micro-topologies rather than surface roughness (Fig. 3A). The small amounts of carbon impurities contained in Ti6Al4V spherical powder were eliminated, and a trace amount of nitrogen was introduced inevitably, which could be caused by the high temperature and high-energy electron beam during EBM printing (Fig. 3B).

Introducing the four porous structures resulted in significant reductions in the compression moduli and the yield strengths of four *in vivo* scaffolds compared with the solid titanium screw of the same size. However, these scaffolds still maintained adequate mechanical strength, which were tough enough to be the orthopedic implant. (Fig. 3C).

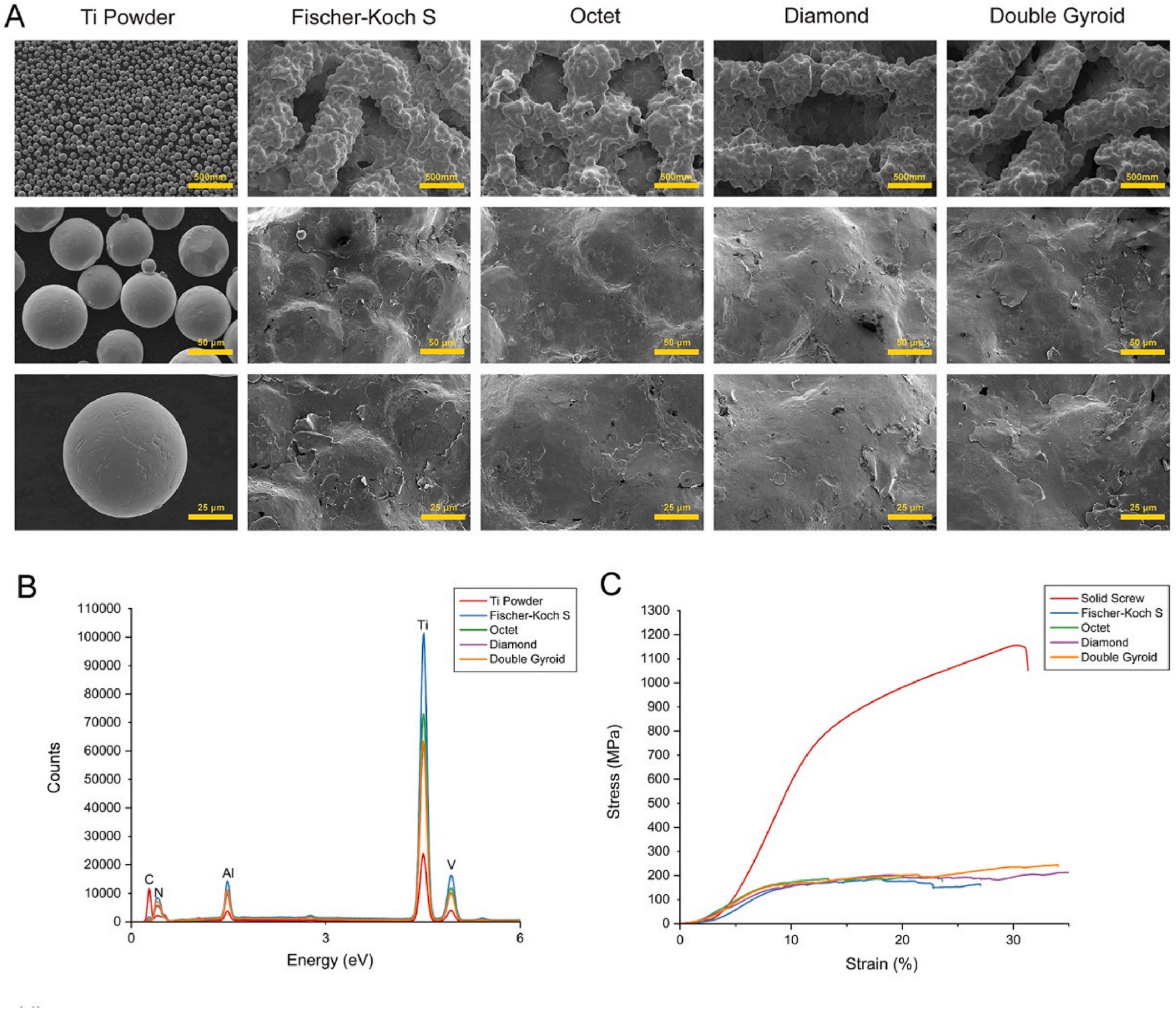

Fig. 3. **(A)** SEM images of Ti6Al4V powder and the four *in vitro* scaffolds observed at different magnifications. **(B)** EDS images of Ti6Al4V powder and the four *in vitro* scaffolds. **(C)** The stress-strain curves of the four *in vivo* scaffolds.

3.3. *Cell proliferation activities*

Live/Dead cell staining results (Fig. 4A) showed that MC3T3-E1 cells could both attach and proliferate in the four kinds of porous scaffolds, which proved their actual bone ingrowth capacities of the four porous scaffolds *in vitro*. In the next five days after seeding, MC3T3-E1 cells kept proliferating, and their proliferation rates were faster from days three–five than from days one–three. Few dead cells could be observed, confirming the ideal biocompatibilities of the four scaffolds in the other aspect. To further detect the specific proliferation rates of MC3T3-E1 cells in the four porous scaffolds, CCK-8 assays were performed (Fig. 4B). On day three, MC3T3-E1 cells seeded on the four scaffolds showed an insignificant difference in proliferation rates, with all four experimental groups exhibiting the similar low-value ranges to the control group (solid scaffold). At day five, MC3T3-E1 proliferation rates primarily increased, especially in the Fischer-Koch S, Octet, and Diamond groups. MC3T3-E1 proliferation rates reached the high values in the Fischer-Koch S, Octet, and Diamond groups compared with that in the Double Gyroid group, whose value was as low as the control group (Fig. 4B).

Besides the above two experiments that demonstrate the possible impacts of the four structure designs on the proliferation rates, the FITC-phalloidin/DAPI staining experiment was performed to analyze the potential influences of the four designs on the cellular morphologies. The stained cytoskeletons and nuclei of the MC3T3-E1 cells have provided clear cellular morphologies on the four kinds of scaffolds (Fig. 4C). MC3T3-E1 cells showed more abundant cellular contacts and interconnections with each other when growing in the Fischer-Koch S and Double Gyroid scaffolds. Therefore, for further improving the stretching and migration capacities of MC3T3-E1, Fischer-Koch S and Double Gyroid structures were proved more suitable to be introduced into the Ti6Al4V scaffolds.

3.4. *Alizarin Red S staining*

The extracellular calcium depositions in the four kinds of scaffolds secreted by MC3T3-E1 cells were stained using Alizarin Red S solution (Fig. 5A). The OD values of CPC solutions in the four experimental

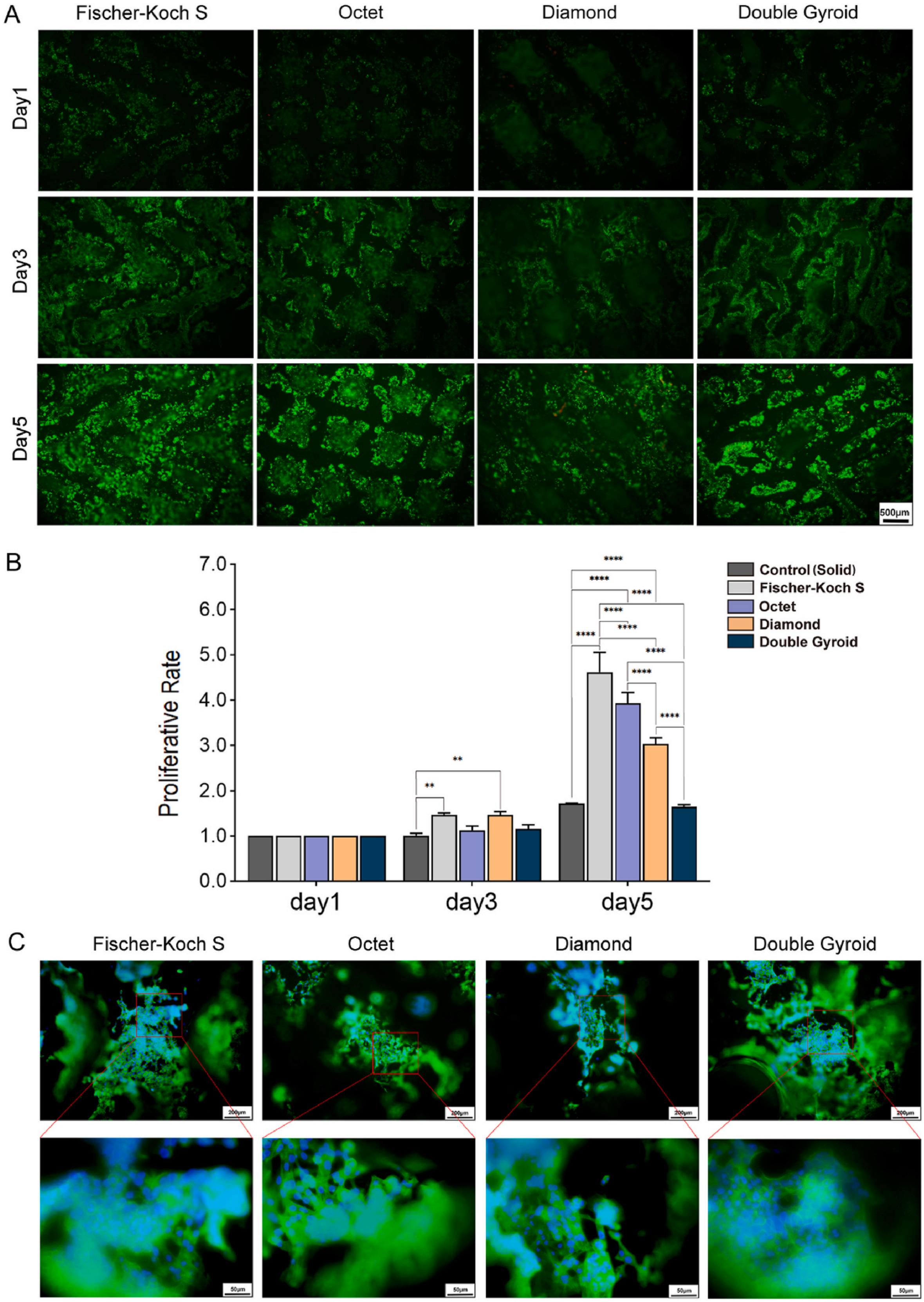

Fig. 4. **(A)** Live/dead cell staining of MC3T3-E1 cells seeded on the four *in vitro* scaffolds, which proliferated for 1, 3, and 5 days. Live cells were stained green, while dead cells were stained red (a small amount). **(B)** MC3T3-E1 cell proliferative rates of the four experimental groups were detected via CCK-8 assays. **(C)** FITC-phalloidin/DAPI staining of MC3T3-E1 cells proliferating on the four *in vitro* scaffolds at day three. Cell cytoskeletons were stained green by FITC-phalloidin, and cell nuclei were stained blue by DAPI. (**$p < 0.01$ and ****$p < 0.0001$).

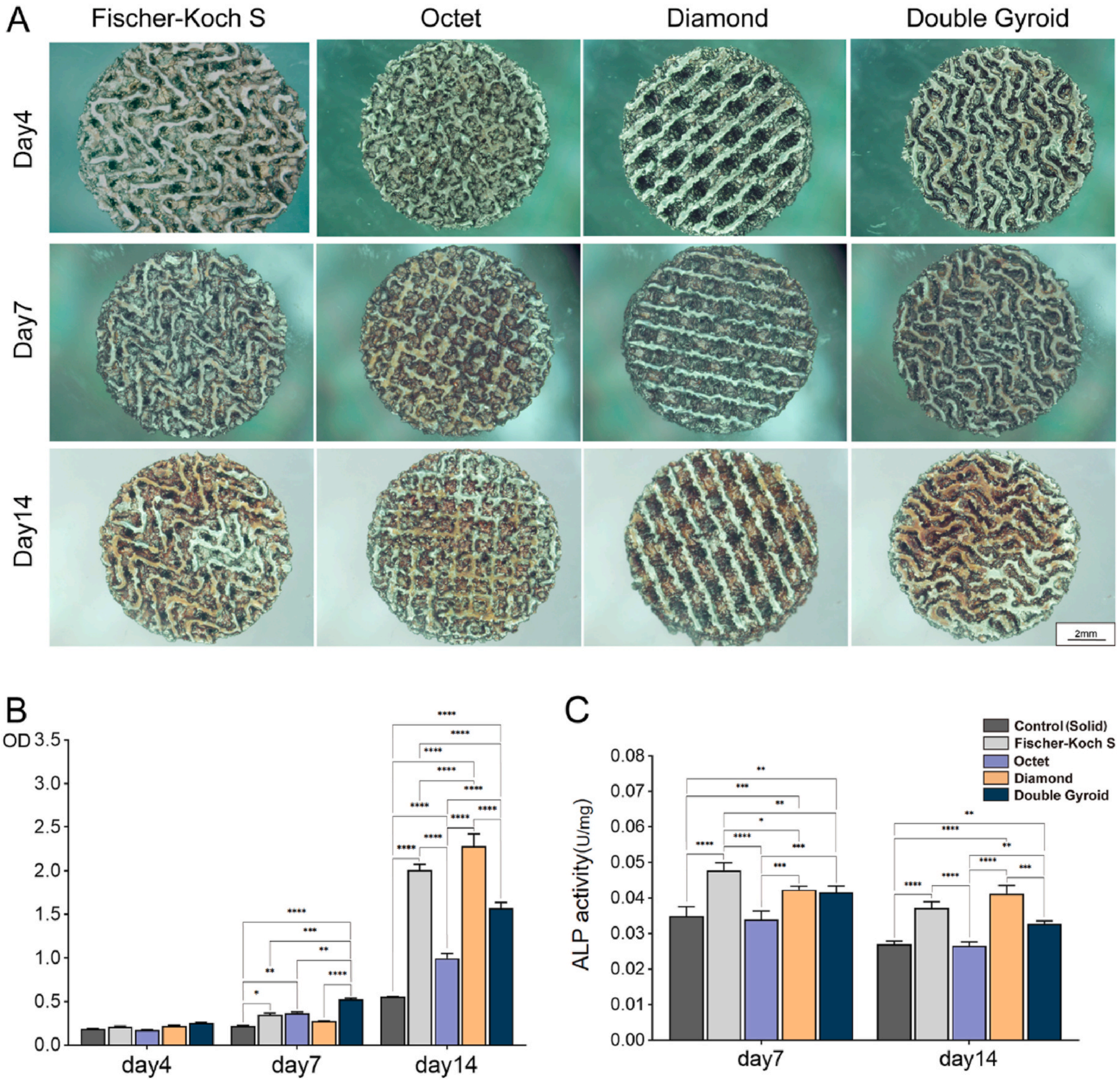

Fig. 5. **(A)** The gross view and **(B)** quantitative analysis of Alizarin Red S staining results. The brown spots on the *in vitro* scaffolds were the stained extracellular calcium deposition, whose quantities were evaluated via the OD values of CPC solutions. **(C)** ALP activity levels in MC3T3-E1 cells seeded on the four kinds of *in vitro* scaffolds. (*$p < 0.05$, **$p < 0.01$, ***$p < 0.001$, and ****$p < 0.0001$).

groups were also detected (Fig. 5B). In the first week of osteogenic differentiation culturing, the content of extracellular calcium deposition in the four scaffolds was low without a significant difference while significantly increasing from day 7 to day 14. The Fischer-Koch S, Diamond, and Double Gyroid groups produced more extracellular calcium deposition than the Octet and control groups.

3.5. ALP test

ALP activities of the MC3T3-E1 cells seeded on the four scaffolds were detected (Fig. 5C). On day seven, ALP activities were higher in the Fischer-Koch S, Diamond, and Double Gyroid groups. The highest value was observed in the Fischer-Koch S group, and the lowest were in the Octet and control groups. On day 14, ALP activities were higher in the Fischer-Koch S and Diamond groups. The highest value was observed in the Diamond group, and the lowest were in the Octet and control groups as well. ALP activities of the five groups decreased minorly from day 7 to day 14, and ALP activities of the Octet and control groups have remained at the lowest level among the five groups.

3.6. RT-PCR assay

Through the procedure of the RT-PCR test introduced in Section 2.5.5, the osteogenesis-related gene expression levels (ALP, OCN, OPN, and Runx-2) in the MC3T3-E1 cells seeded on the four porous scaffolds were finally detected (Fig. 6A–D). ALP and Runx-2 expressions were higher in the Fischer-Koch S, Diamond, and Double Gyroid groups. Meanwhile, OCN and OPN expressions were higher in the Fischer-Koch S group. From days 7–14, the overall OCN and OPN expression levels presented an increasing trend, and the overall ALP and Runx-2 expression levels presented a decreasing trend. Remarkably, the osteogenesis-related gene expression levels among the four groups were all lowest in the Octet group.

3.7. Micro-CT analysis

With the technique of micro-CT, 3D images of medial femoral condyle defects reconstructed by the four porous scaffolds and the one solid scaffold were entirely generated, showing the distributions of new bone tissues in the corresponding defects (Fig. 7A). New bone tissues

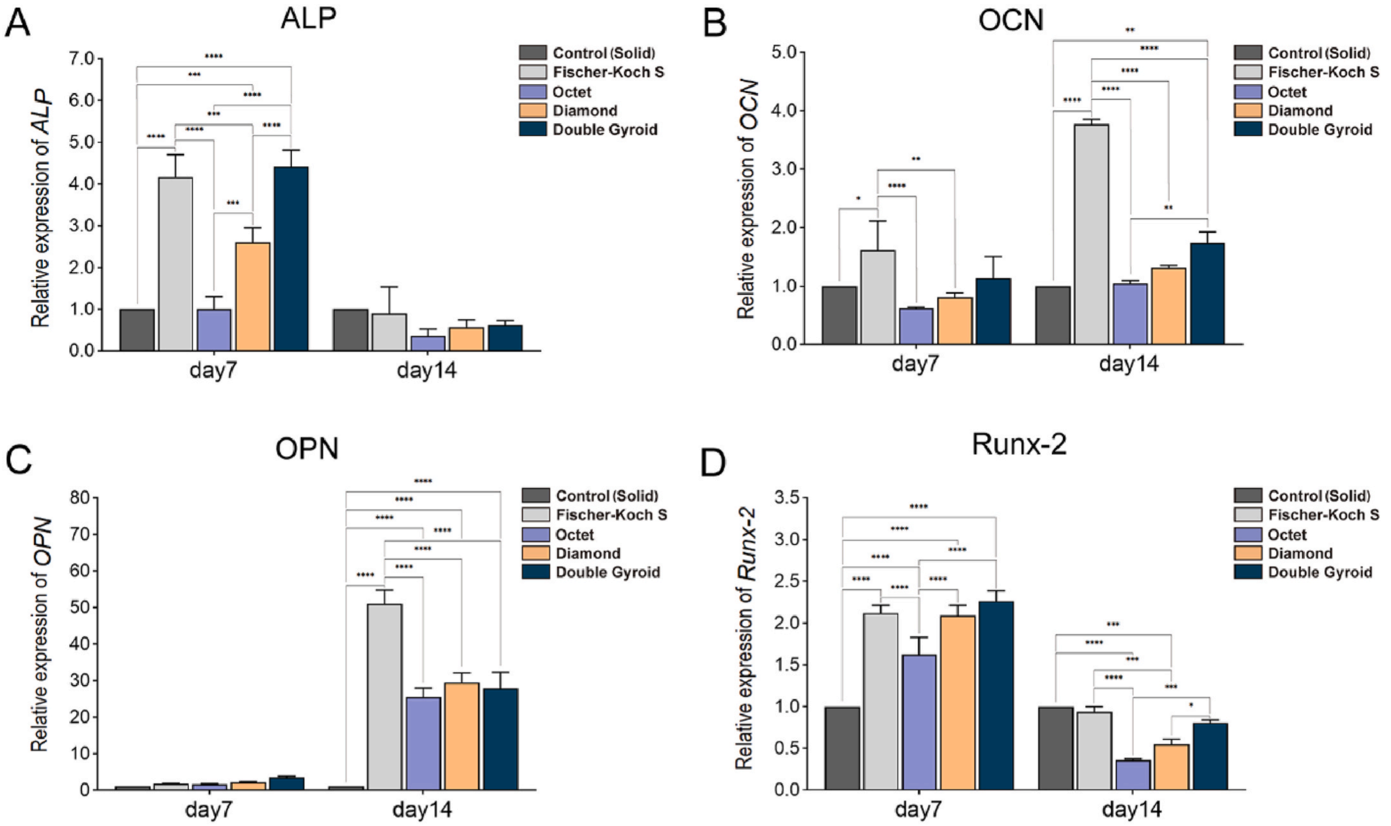

Fig. 6. The expression levels of several osteogenesis-related genes in MC3T3-E1 cells seeded on the four *in vitro* scaffolds. ($*p < 0.05$, $**p < 0.01$, $***p < 0.001$, and $****p < 0.0001$).

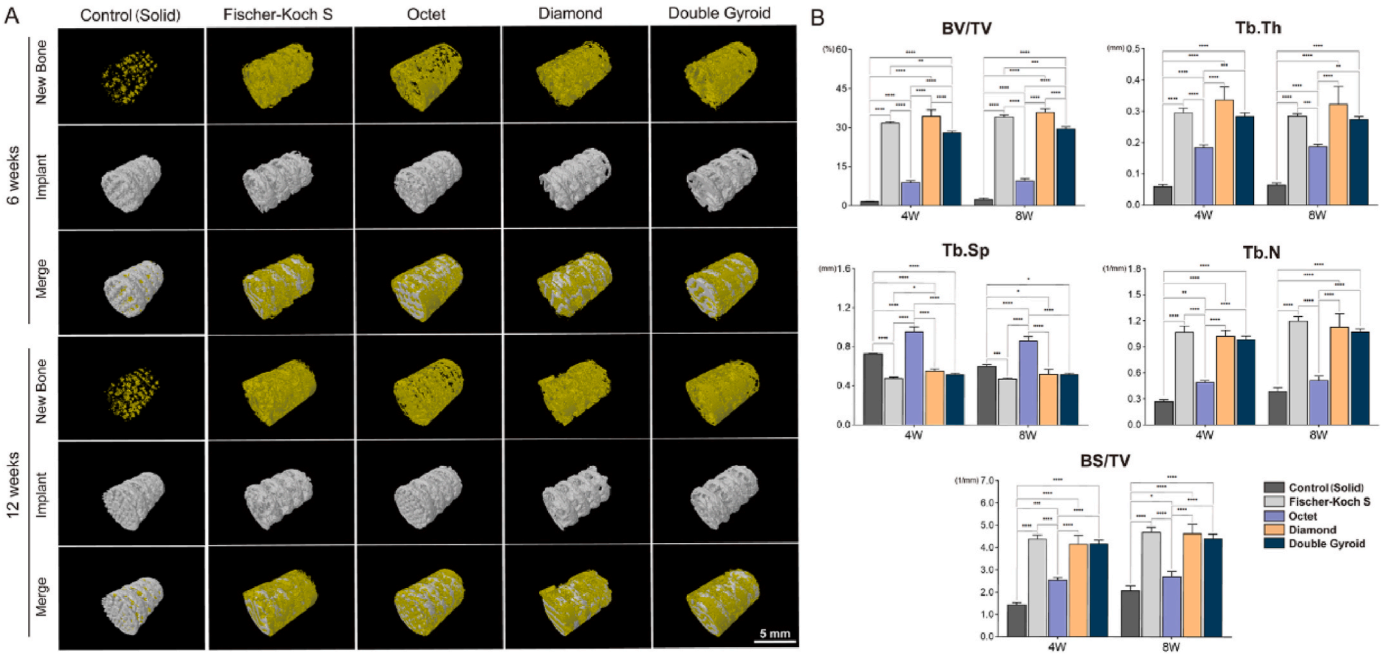

Fig. 7. **(A)** Micro-CT results of *in vivo* femoral condyle defects reconstructed by the four scaffolds. The yellow domains were the regenerated bone tissue, and the grey domains were the four scaffolds implanted. **(B)** The quantitative analyses of the osteogenesis indices, including BV/TV, Tb. Th, Tb. Sp, Tb. N, and BS/TV were used to evaluate the qualities of new bone. ($*p < 0.05$, $**p < 0.01$, $***p < 0.001$, and $****p < 0.0001$).

(the yellow domains) were regenerated around the scaffolds (the grey domains), with some parts growing and infiltrating into the pores of the scaffolds successfully. To analyze the quality differences of the new bone tissues between the four experimental groups, a series of osteogenesis indices (BV/TV, Tb. Th, Tb. Sp, Tb. N, and BS/TV) were calculated (Fig. 7B). BV/TV and Tb. Th were used to assess the total volume and the mean thickness of the new bone trabeculae, whose values were high in Fischer-Koch S, Diamond, and Double Gyroid groups while were low in Octet and control groups relatively. The much higher values of the two indices were found in the Fischer-Koch S and Diamond groups, which means that these two structures could induce more bone regeneration *in vivo* compared with the other structures.

Tb. Sp index represents the mean width of medullary space between the new bone trabeculae, whose values were lower in Fischer-Koch S, Diamond, and Double Gyroid groups (lowest in the Fischer-Koch S group specifically) while were higher in Octet and control groups. Tb. N index represents the average trabecular number per millimeter of the new bone, and the BS/TV index was used to assess the total surface area of the new bone trabeculae. Tb. N and BS/TV values were higher in the Fischer-Koch S, Diamond, and Double Gyroid (highest in the Fischer-Koch S group specifically) but were lower in Octet and control groups. The above results of Tb. Sp, Tb. N and BS/TV indices revealed that Fischer-Koch S, Diamond, and Double Gyroid structures could significantly induce the denser bone tissue with a larger surface area *in vivo*.

3.8. Tissue section analysis

Fig. 8A shows the Hematoxylin and Eosin staining results of the four groups of scaffolds. The red areas represent the regenerated collagen connective tissues in the defects, mainly composed of bone and cartilage tissues. To further explore the compositions of the collagen connective tissues, Toluidine blue staining was performed (Fig. 8B). The light/dark blue areas represent the regenerated bone tissues, and the reddish-purple areas represent the regenerated cartilage tissues. Based on the above outcomes of tissue section staining, the regenerated collagen connective tissues in the different samples consisted almost entirely of the bone tissues, and only a few of the cartilage tissue components could be spotted in the Fischer-Koch S and Double Gyroid scaffolds. Among the four groups of scaffolds, more bone was newly formed in Fischer-Koch S, Diamond, and Double Gyroid groups, and more bone tissues were contacted and integrated tightly with these three scaffolds. No prominent inflammatory tissue was observed in either of the four groups, demonstrating the ideal biocompatibility of the four kinds of scaffolds. At week 12 after implantation, Haversian bone structures could be found in the Fischer-Koch S, Diamond, and Double Gyroid groups, further confirming the advantages of these three scaffolds in promoting bone maturation.

4. Discussion

Titanium metallic screw is a common implant applied in orthopedics due to the superior mechanical strength and the biocompatibility of Ti material [65–67]. Although the traditional titanium screw is often manufactured with a simple solid design, it causes stress shielding and postoperative loosening [8,9]. With the extra porous structures introduced, the elastic modulus of the screw could decrease tremendously to reduce stress shielding. The regenerated bone tissue in the implanted site could grow into the pores and integrate with the implanted screw, which would notably improve the long-term fixation effect of the screw. For investigating the appropriate porous structure types to promote osteogenesis of the titanium screw greatly, we tentatively selected four classic additive manufacturing porous designs (Fischer-Koch S, Octet, Diamond, and Double Gyroid), which were introduced into the experimental titanium scaffolds for further biological studies *in vitro* and *in vivo*. These four kinds of topology-optimized scaffolds have been fabricated successfully with the EBM technology. After several *in vitro* and *in vivo* experiments with these scaffolds, the potential influences of their structure designs on bone regeneration were fully exposed, providing some clues for the topological optimization of the porous titanium screw used in orthopedics in the future.

For comparing the differences in bone regeneration capacities between the porous titanium scaffolds under the four different structure designs, the proliferative and osteogenic differential activities of osteoblasts (MC3T3-E1) growing in those porous scaffolds were examined in detail. The Live/Dead cell staining and CCK-8 assay results indicated that osteoblasts proliferated was increased in the Fischer-Koch S scaffold. Moreover, FITC-phalloidin/DAPI staining results revealed that more abundant cytoskeletons and stretched morphologies were spotted in the Fischer-Koch S and Double Gyroid groups, demonstrating that these two structures could primarily improve osteoblast migration and infiltration. These three experiments can effectively identify and select the Fischer-Koch S structure to optimize osteoblast proliferation. Moreover, the calcium deposition contents, ALP activities, and the osteogenesis-related gene expressions (ALP, OCN, OPN, Runx-2) of the osteoblasts growing in the four kinds of scaffolds were assessed via Alizarin Red S staining, ALP assay, and RT-PCR, revealing the different capacities of the four structures on osteogenic differentiation. Runx-2 is a crucial regulatory factor in osteogenic differentiation that upregulates many other osteogenesis-related genes, including ALP, OPN, and OCN [68,69]. ALP is crucial in providing phosphate via pyrophosphate hydrolysis (a hydroxyapatite propagation inhibitor) [68]. The generated phosphate is bonded with calcium, forming hydroxyapatite crystals [70]. The newly formed hydroxyapatite crystals are then regulated and remodeled by OPN and OCN, thus accelerating hydroxyapatite crystal maturation [71–76]. Therefore, these four genes are critical for osteogenic differentiation detection. Herein, more calcium deposition contents and higher ALP activities were found in the Fischer-Koch S, Diamond, and Double Gyroid groups. Runx-2 expressions were higher in the Fischer-Koch S, Diamond, and Double Gyroid scaffolds. OCN and OPN expressions were higher in the Fischer-Koch S scaffold, and the ALP expressions in the Fischer-Koch S, Diamond, and Double Gyroid.

Furthermore, *in vivo* micro-CT and tissue section analysis experiments demonstrated the higher bone regeneration capacities of the Fischer-Koch S, Diamond, and Double Gyroid scaffolds. The potential enhancement of osteogenic differential capacities in porous titanium scaffolds can be achieved by screening Fischer-Koch S, Diamond, and Double Gyroid structures. Notably, the Fischer-Koch S scaffold demonstrates exceptional osteogenic differential capacity across all aspects. The overall outcomes of osteoblast proliferation activities confirmed that the Fischer-Koch S structure was the most appropriate to be introduced to increase the bone regeneration capacity of the porous titanium scaffold. The bioeffects of this structure on promoting bone regeneration were the most general and relatively stable among the four kinds of structures.

The four kinds of structures used for titanium implant optimization showed apparent variations in bone regeneration, and Fischer-Koch S structure was proved superior for improving bone tissue regrowth. Therefore, the titanium screw applied in orthopedics should be designed into the Fischer-Koch S structure (Fig. 9A). Except for the application in fracture internal fixation, titanium screw was extensively employed in other orthopedic surgeries, for example the screw-rod fixation system implantation and the dental prosthesis implantation [77–79]. In these clinical situations, porous titanium screws should better be used to substitute the traditional solid screws, and the Fischer-Koch S structure should be introduced to enhance their long-term fixation effects ulteriorly. In addition to the above screws, the Fischer-Koch S structure could be introduced into other orthopedic implants, including the defect implants in mandibular reconstruction, the bone plates, and the interbody fusion cages used in discectomy (Fig. 9B) [80]. These screws and implants can be manufactured with Ti material and EBM technique as well as other metals (e.g., Mg and Zn), polymeric materials (e.g., polyglycolic acid and polyetheretherketone), and printing techniques (e.g., selective laser sintering and stereo lithography apparatus techniques). Introducing the Fischer-Koch S metamaterial into these implants will significantly improve their osteogenesis capacities.

Compared with the Octet and solid structures, Fischer-Koch S, Diamond, and Double Gyroid structures were more effective in improving bone regeneration, all belonging to the TPMS structure category. The typical characteristics of TPMS structure are the mean surface curvature

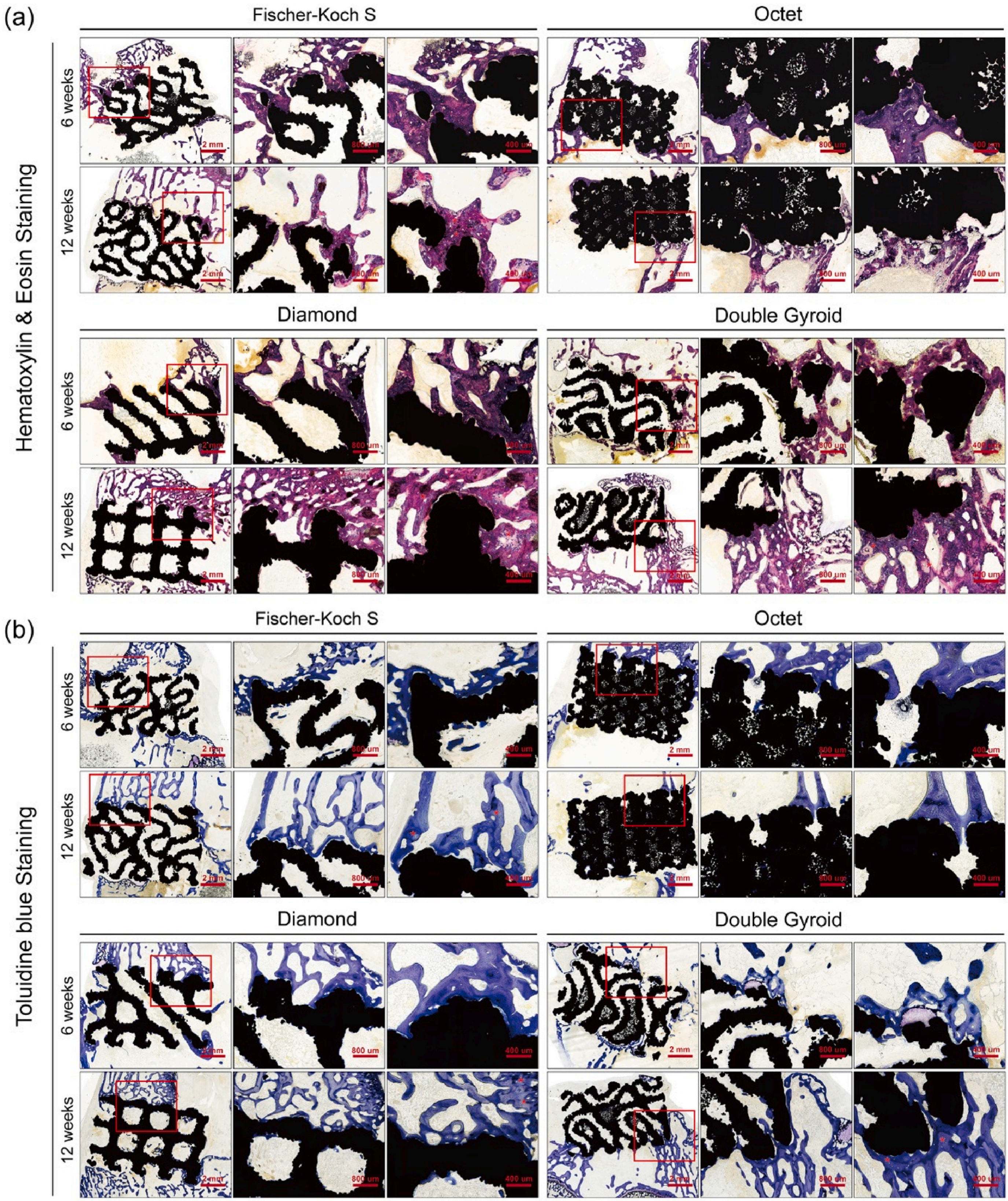

Fig. 8. **(A)** Hematoxylin and Eosin and **(B)** Toluidine blue staining results of the *in vivo* femoral condyle defects reconstructed by the four scaffolds. Red asterisks in the figures marked out several locations of Haversian bone structures, indicating the regenerated bone tissue maturation.

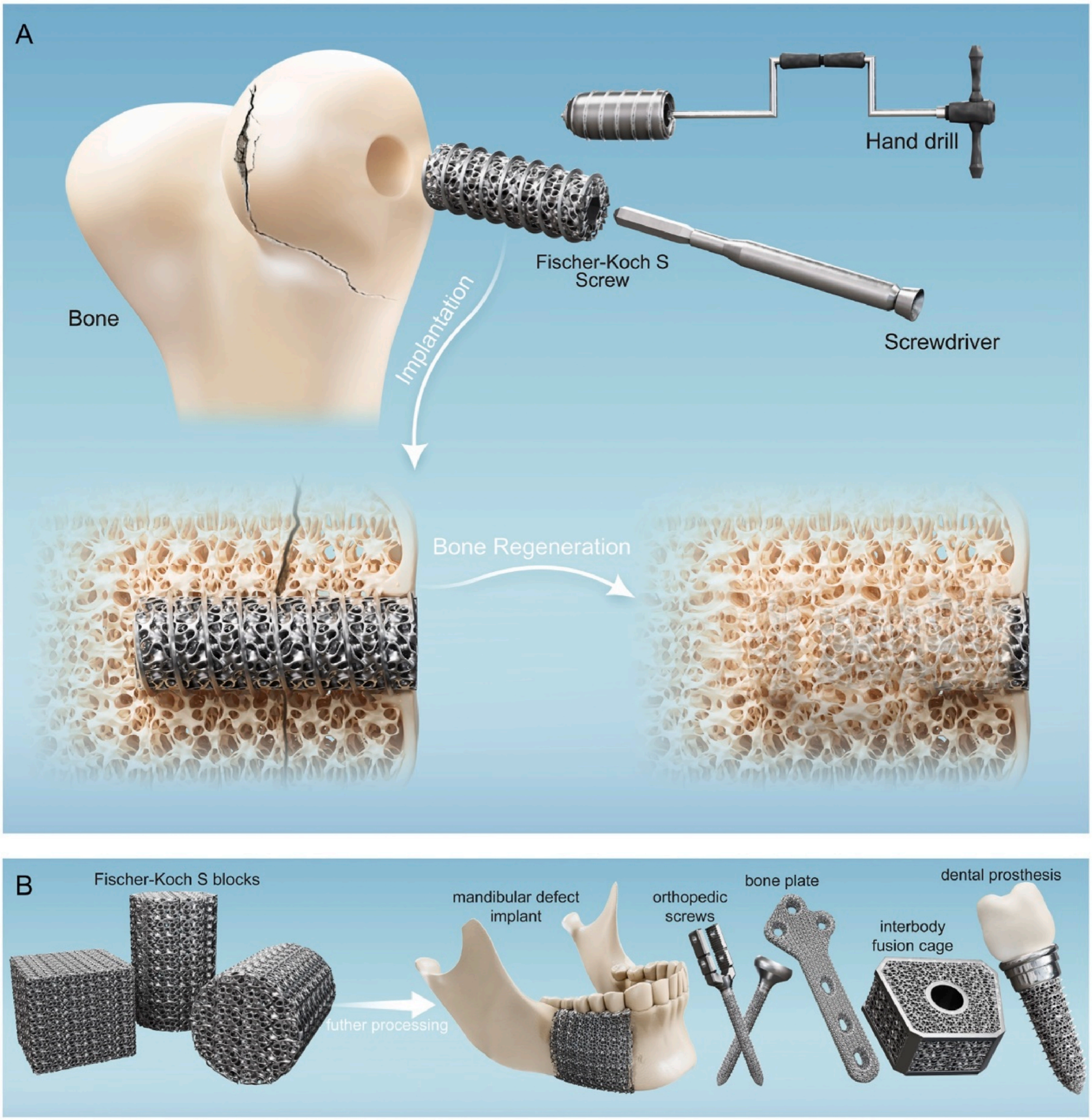

Fig. 9. **(A)** The topology-optimized titanium screw applied in the internal fixation of fracture. With the porous structure introduced, the long-term fixation effect of the screw after surgery could get promoted continuously as more bone tissue regrow and infiltrate into the screw. **(B)** The potential application prospects of Fischer-Koch S porous structure in the mandibular defect implant, the orthopedic screws, the bone plate, the interbody fusion cage used in the field of spine, and the dental prosthesis used in the field of dentistry.

of zero and the absence of surface self-intersection [47,81], which could be the possible reason for its unique capacity for bone tissue regeneration. As a classic archetype topology structure, Octet is composed of a triangular structure whose inner neighboring struts intersect at 45° [48,49]. This structure could be inferior for bone tissue regeneration comparatively, whose introduction brought a weak bone regeneration capacity of the metallic screw that was similar to the traditional solid design.

5. Conclusion

Unlike traditional solid design, porous structure design was more advantageous to be applied in the metallic orthopedic screw for improving its long-term fixation effect after implantation. With the porous structure being introduced, the screw modulus was decreased into the reasonable value range of trabecular bone tissue, which would alleviate postoperative bone deterioration near the implanted screw by reducing stress shielding problems. Furthermore, porous tissue structure could bring more space for the infiltration and integration of regenerated bone tissue *in situ*, elevating the stabilities and fixation strengths of the screw to a higher level. This study tentatively selected and used four classic additive manufacturing porous designs (Fischer-Koch S, Octet, Diamond, Double Gyroid) in orthopedic implants, whose capacities for bone regeneration were examined via multiple *in vitro* and *in vivo* experiments. Among these four structures, the Fischer-Koch S structure was most effective one for bone regeneration, and the Octet structure was the least effective one in comparison.

Funding

This study was supported by the Department of Science and Technology of Jilin Province [grant numbers 20210204104YY, YDZJ202201ZYTS135, 20200404202YY]; the Bethune plan of Jilin University [grant numbers 2023B08, 2023B10]; the National Key R&D

Program of China [No. 2018YFB1105100]; the Scientific Development Program of Jilin Province [grant numbers YDZJ202301ZYTS031, YDZJ202301ZYTS032, YDZJ202201ZYTS281, 20240402016]; the Jilin Province Development and Reform Commission, P.R.C [grant number 2018C010]; the Tianhua Health Foundation of Jilin Province [grant number Z60979288864140018]; the Jilin Province Health Science and Technology Capacity Improvement Plan [grant number 2023LC018]; and the National Innovative Entrepreneurship Training Program for Undergraduates [grant number 202210183323].

Ethics approval and consent to participate

All the relevant experimental procedures strictly followed the laws, regulations, and stipulations of animal ethics, which were approved by the Laboratory Teaching Center of Basic Medicine, Jilin University (approval number: No.2023430).

CRediT authorship contribution statement

Wangwang Luo: Writing – original draft, Investigation. **Yang Wang:** Data curation, Conceptualization. **Zhonghan Wang:** Supervision, Conceptualization. **Jianhang Jiao:** Supervision, Methodology. **Tong Yu:** Resources, Project administration. **Weibo Jiang:** Resources, Project administration. **Mufeng Li:** Validation, Methodology. **Han Zhang:** Supervision. **Xuqiang Gong:** Data curation. **Bo Chao:** Methodology. **Shixian Liu:** Validation. **Xuhui Wu:** Validation. **Jincheng Wang:** Supervision, Methodology, Funding acquisition. **Minfei Wu:** Writing – review & editing, Supervision, Funding acquisition, Conceptualization.

Declaration of competing interest

The authors declare that they have no known competing financial interests or personal relationships that could have appeared to influence the work reported in this paper.

Data availability

Data will be made available on request.

References

[1] B.A. Bean, N.A. Smyth, P. Abbasi, B.G. Parks, W.C. Hembree, Biomechanical comparison of hook plate vs headless compression screw fixation of large fifth metatarsal base avulsion fractures, Foot Ankle Int. 42 (1) (2021) 89–95.
[2] C.W. Chang, Y.N. Chen, H.C. Chang, C.T. Li, Biomechanical comparison of different screw-included angles in crossing screw fixation for transverse patellar fracture in level walking: a quasi-dynamic finite element study, J. Orthop. Surg. Res. 18 (1) (2023).
[3] H. Basar, B. Basar, O. Başçi, O.M. Topkar, B. Erol, C. Tetik, Comparison of treatment of oblique and spiral metacarpal and phalangeal fractures with mini plate plus screw or screw only, Arch. Orthop. Trauma Surg. 135 (4) (2015) 499–504.
[4] A.M. Wu, W.F. Ni, Z.X. Shao, X.J. Kong, N.F. Tian, Y.X. Huang, Z.K. Lin, H.Z. Xu, Y. L. Chi, Percutaneous posterior transdiscal oblique screw fixation with lateral interbody fusion: a radiological and cadaveric study, Eur. Spine J. 24 (4) (2015) 852–858.
[5] L. Natera, M. Valera, E.M. Gómez, N. Ibañez, X. Crusi, R. Sancho, Survival of hydroxyapatite-coated cups: acetabular screws involve a lower rate of revision surgery due to aseptic loosening, Hip Int. 27 (2) (2017) 153–161.
[6] J. Litak, M. Szymoniuk, W. Czyzewski, Z. Hoffman, J. Litak, L. Sakwa, P. Kamieniak, Metallic implants used in lumbar interbody fusion, Materials 15 (10) (2022) 23.
[7] N. Ipek, I. Mutlu, Production of Mg-Ca-Zn-Zr-Cu alloy for resorbable compression screw in bone fixation applications, Mater. Technol. 36 (5) (2021) 270–278.
[8] K. Haase, G. Rouhi, Prediction of stress shielding around an orthopedic screw: using stress and strain energy density as mechanical stimuli, Comput. Biol. Med. 43 (11) (2013) 1748–1757.
[9] S. Kuroda, Y. Nishii, S. Okano, K. Sueishi, Stress distribution in the mini-screw and alveolar bone during orthodontic treatment: a finite element study analysis, J. Orthod. 41 (4) (2014) 275–284.
[10] L.D. Song, Effects of exercise or mechanical stimulation on bone development and bone repair, Stem Cell. Int. 2022 (2022) 10.
[11] Y.Y. Sun, B. Wan, R.X. Wang, B.W. Zhang, P. Luo, D.D. Wang, J.J. Nie, D.F. Chen, X.B. Wu, Mechanical stimulation on mesenchymal stem cells and surrounding microenvironments in bone regeneration: regulations and applications, Front. Cell Dev. Biol. 10 (2022) 17.
[12] M. Torabi, S. Khorramymehr, M. Nikkhoo, M. Rostami, The role of orthopedic screws threads properties on the success of femoral fracture fixation, Proc. IME C J. Mech. Eng. Sci. 236 (17) (2022) 9419–9430.
[13] M. Be'ery-Lipperman, A. Gefen, A method of quantification of stress shielding in the proximal femur using hierarchical computational modeling, Comput. Methods Biomech. Biomed. Eng. 9 (1) (2006) 35–44.
[14] S. Hosin, D. Vermesan, R. Prejbeanu, D. Crisan, M. Al-Qatawneh, D. Pop, M. Mioc, F. Bratosin, B. Feciche, K. Hemaswini, M.L. Moise, C. Dumitru, V. Bloanca, C. N. Pilut, Avoiding the removal of syndesmotic screws after distal tibiofibular diastasis repair: a benefit or a drawback? J. Clin. Med. 11 (21) (2022).
[15] X.L. Wu, J.W. Shi, J.Y. Wu, Y.Q. Cheng, K.W. Peng, J.T. Chen, H. Jiang, Pedicle screw loosening: the value of radiological imagings and the identification of risk factors assessed by extraction torque during screw removal surgery, J. Orthop. Surg. Res. 14 (2019).
[16] M. Oberst, G. Konrad, G.W. Herget, A. El Tayeh, N.P. Suedkamp, Novel endoscopic sacroiliac screw removal technique: reduction of intraoperative radiation exposure, Arch. Orthop. Trauma Surg. 134 (11) (2014) 1557–1560.
[17] Y. Naidubabu, G.M. Rao, K. Rajasekhar, B.R. Sunil, Design and simulation of polymethyl methacrylate-titanium composite bone fixing plates using finite element analysis: optimizing the composition to minimize the stress shielding effect, Proc. IME C J. Mech. Eng. Sci. 231 (23) (2017) 4402–4412.
[18] S.A. Naghavi, M. Tamaddon, P. Garcia-Souto, M. Moazen, S. Taylor, J. Hua, C. Z. Liu, A novel hybrid design and modelling of a customised graded Ti-6Al-4V porous hip implant to reduce stress-shielding: an experimental and numerical analysis, Front. Bioeng. Biotechnol. 11 (2023) 20.
[19] D. Wu, P. Isaksson, S.J. Ferguson, C. Persson, Young's modulus of trabecular bone at the tissue level: a review, Acta Biomater. 78 (2018) 1–12.
[20] J. Tan, E. Natarajan, W. Lim, S. Ramesh, C. Ang, S. Parasuraman, D.K.J. Singh, Effects of bone-plate materials on the healing process of fractured tibia bone under time-varying conditions: a finite element analysis, Mater. Res. Express 8 (9) (2021) 19.
[21] L. de Ruiter, K. Rankin, M. Browne, A. Briscoe, D. Janssen, N. Verdonschot, Decreased stress shielding with a PEEK femoral total knee prosthesis measured in validated computational models, J. Biomech. 118 (2021) 8.
[22] V.K. Meena, P. Kalra, R.K. Sinha, Finite element study on the influence of pore size and structure on stress shielding effect of additive manufactured spinal cage, Comput. Methods Biomech. Biomed. Eng. 25 (5) (2022) 566–577.
[23] B.L. Liu, H.Z. Wang, N.Z. Zhang, M. Zhang, C.K. Cheng, Femoral stems with porous lattice structures: a review, Front. Bioeng. Biotechnol. 9 (2021) 19.
[24] M. Sun, H.F. Shao, H.B. Xu, X.F. Yang, M.Y. Dong, J.X. Gong, M.F. Yu, Z.R. Gou, Y. He, A. Liu, H.M. Wang, Biodegradable intramedullary nail (BIN) with high-strength bioceramics for bone fracture, J. Mater. Chem. B 9 (4) (2021) 15.
[25] Q.M. Tian, L. Rivera-Castaneda, H.N. Liu, Optimization of of nano-hydroxyapatite/poly(lactic-*co*-glycolic acid) coatings on magnesium substrates using one-step electrophoretic deposition, Mater. Lett. 186 (2017) 12–16.
[26] C. Domínguez-Trujillo, F. Ternero, J.A. Rodríguez-Ortiz, S. Heise, A.R. Boccaccini, J. Lebrato, Y. Torres, Bioactive coatings on porous titanium for biomedical applications, Surf. Coat. Technol. 349 (2018) 584–592.
[27] C. Domínguez-Trujillo, F. Ternero, J.A. Rodríguez-Ortiz, J.J. Pavón, I. Montealegre-Meléndez, C. Arévalo, F. García-Moreno, Y. Torres, Improvement of the balance between a reduced stress shielding and bone rit ingrowth by bioactive coatings onto porous titanium substrates, Surf. Coat. Technol. 338 (2018) 32–37.
[28] A.C. Jones, C.H. Arns, A.P. Sheppard, D.W. Hutmacher, B.K. Milthorpe, M. A. Knackstedt, Assessment of bone ingrowth into porous biomaterials using MICRO-CT, Biomaterials 28 (15) (2007) 2491–2504.
[29] C. Wu, J.G. Fang, A. Entezari, G.Y. Sun, M.V. Swain, Y.N. Xu, G.P. Steven, Q. Li, A time-dependent mechanobiology-based topology optimization to enhance bone growth in tissue scaffolds, J. Biomech. 117 (2021).
[30] H. Tiainen, J.C. Wohlfahrt, A. Verket, S.P. Lyngstadaas, H.J. Haugen, Bone formation in TiO_2 bone scaffolds in extraction sockets of minipigs, Acta Biomater. 8 (6) (2012) 2384–2391.
[31] L.Z. Wang, H.W. Huang, H. Yuan, Y. Yao, J.H. Park, J.L. Liu, X.Z. Geng, K. Zhang, S.J. Hollister, Y.B. Fan, *In vitro* fatigue behavior and in vivo osseointegration of the auxetic porous bone screw, Acta Biomater. 170 (2023) 185–201.
[32] M. Al Deeb, A.A. Aldosari, S. Anil, Osseointegration of tantalum trabecular metal in titanium dental implants: histological and micro-CT study, J. Funct. Biomater. 14 (7) (2023) 12.
[33] A.R. Edelmann, D. Patel, R.K. Allen, C.J. Gibson, A.M. Best, S. Bencharit, Retrospective analysis of porous tantalum trabecular metal-enhanced titanium dental implants, J. Prosthet. Dent 121 (3) (2019) 404–410.
[34] N. Alan, K.E. Lee, J.J. Zhou, H. Farber, J.D. DiDomenico, L.K. O'Neill, J.D. Turner, J.S. Uribe, Bilateral sacroiliac joint fusion in long constructs using self-harvesting porous S2-alar iliac screws with an integrated tulip: technical considerations and early clinical and radiographic experience, Neurosurg. Focus 55 (1) (2023) 6.
[35] J. Li, X.L. Cui, G.J. Hooper, K.S. Lim, T.B.F. Woodfield, Rational design, bio-functionalization and biological performance of hybrid additive manufactured titanium implants for orthopaedic applications: a review, J. Mech. Behav. Biomed. Mater. 105 (2020) 18.
[36] H.J. Cao, L.F. Feng, Z.X. Wu, W.T. Hou, S.J. Li, Y.L. Hao, L. Wu, Effect of low-intensity pulsed ultrasound on the biological behavior of osteoblasts on porous titanium alloy scaffolds: an in vitro and in vivo study, Mater. Sci. Eng., C 80 (2017) 7–17.

[37] Y.S. Cho, J.S. Lee, M.W. Hong, S.H. Lee, Y.Y. Kim, Y.S. Cho, Comparative assessment of the ability of dual-pore structure and hydroxyapatite to enhance the proliferation of osteoblast-like cells in well-interconnected scaffolds, Int. J. Precis. Eng. Manuf. 19 (4) (2018) 605–612.

[38] Q. Zhang, H.X. Lu, N. Kawazoe, G.P. Chen, Preparation of collagen scaffolds with controlled pore structures and improved mechanical property for cartilage tissue engineering, J. Bioact. Compat, Polymers 28 (5) (2013) 426–438.

[39] X.M. Shi, A. Nommeots-Nomm, N.M. Todd, A. Devlin-Mullin, H. Geng, P.D. Lee, C. A. Mitchell, J.R. Jones, Bioactive glass scaffold architectures regulate patterning of bone regeneration *in vivo*, Appl. Mater. Today 20 (2020) 11.

[40] H. Zhu, M. Li, X.L. Huang, D.H. Qi, L.P. Nogueira, X. Yuan, W.B. Liu, Z.H. Lei, J. W. Jiang, H.L. Dai, J. Xiao, 3D printed tricalcium phosphate-bioglass scaffold with gyroid structure enhance bone ingrowth in challenging bone defect treatment, Appl. Mater. Today 25 (2021) 15.

[41] C.N. Sun, E.C. Dong, J.Y. Chen, J.B. Zheng, J.F. Kang, Z.M. Jin, C.Z. Liu, L. Wang, D.C. Li, The promotion of mechanical properties by bone ingrowth in additive-manufactured titanium scaffolds, J. Funct. Biomater. 13 (3) (2022) 16.

[42] W.W. Luo, Y. Wang, Q. Han, Z.H. Wang, J.H. Jiao, X.Q. Gong, Y. Liu, A.B. Zhang, H. Zhang, H. Chen, J.C. Wang, M.F. Wu, Advanced strategies for constructing interfacial tissues of bone and tendon/ligament, J. Tissue Eng. 13 (2022) 31.

[43] D.J. Yoo, Porous scaffold design using the distance field and triply periodic minimal surface models, Biomaterials 32 (31) (2011) 7741–7754.

[44] A. Karakoç, RegionTPMS - region based triply periodic minimal surfaces (TPMS) for 3-D printed multiphase bone scaffolds with exact porosity values, SoftwareX 16 (2021) 8.

[45] H. Chen, Q. Han, C.Y. Wang, Y. Liu, B.P. Chen, J.C. Wang, Porous scaffold design for additive manufacturing in orthopedics: a review, Front. Bioeng. Biotechnol. 8 (2020) 20.

[46] Y.T. Lu, W.Y. Zhao, Z.T. Cui, H.X. Zhu, C.W. Wu, The anisotropic elastic behavior of the widely-used triply-periodic minimal surface based scaffolds, J. Mech. Behav. Biomed. Mater. 99 (2019) 56–65.

[47] Y.T. Lu, Y. Huo, J.A. Zou, Y.C. Li, Z.Y. Yang, H.X. Zhu, C.W. Wu, Comparison of the design maps of TPMS based bone scaffolds using a computational modeling framework simultaneously considering various conditions, Proc. Inst. Mech. Eng. Part H-J. Eng. Med. 236 (8) (2022) 1157–1168.

[48] L.P. Wang, Q. Chen, P. Yarlagadda, F.P. Zhu, Q.W. Li, Z.Y. Li, Single-parameter mechanical design of a 3D-printed octet truss topological scaffold to match natural cancellous bones, Mater. Des. 209 (2021) 12.

[49] S. Arabnejad, R.B. Johnston, J.A. Pura, B. Singh, M. Tanzer, D. Pasini, High-strength porous biomaterials for bone replacement: a strategy to assess the interplay between cell morphology, mechanical properties, bone ingrowth and manufacturing constraints, Acta Biomater. 30 (2016) 345–356.

[50] M. Nonomura, K. Yamada, T. Ohta, Formation and stability of double gyroid in microphase-separated diblock copolymers, J. Phys.-Condes. Matter 15 (26) (2003) L423–L430.

[51] A. Aksimentiev, M. Fialkowski, R. Holyst, Morphology of surfaces in mesoscopic polymers, surfactants, electrons, or reaction-diffusion systems: methods, simulations, and measurements, in: I. Prigogine, S.A. Rice (Eds.), Advances in Chemical Physics, vol. 121, John Wiley & Sons Inc, Hoboken, 2002, pp. 141–239.

[52] F. Sadeghi, M. Baniassadi, A. Shahidi, M. Baghani, TPMS metamaterial structures based on shape memory polymers: mechanical, thermal and thermomechanical assessment, J. Mater. Res. Technol-JMRT 23 (2023) 3726–3743.

[53] N.V. Viet, N. Karathanasopoulos, W. Zaki, Mechanical attributes and wave propagation characteristics of TPMS lattice structures, Mech. Mater. 172 (2022) 12.

[54] B.M. Cote, W.R. Lenart, C.J. Ellison, V.E. Ferry, Surface structure dependent circular dichroism in single and double gyroid metamaterials, Adv. Opt. Mater. 10 (13) (2022) 10.

[55] Y.T. Lu, L.L. Cheng, Z.Y. Yang, J.Y. Li, H.X. Zhu, Relationship between the morphological, mechanical and permeability properties of porous bone scaffolds and the underlying microstructure, PLoS One 15 (9) (2020) 19.

[56] J. Li, D.S. Chen, H.Q. Luan, Y.Y. Zhang, Y.B. Fan, Numerical evaluation and prediction of porous implant design and flow performance, BioMed Res. Int. 2018 (2018) 13.

[57] I. Maskery, N.T. Aboulkhair, A.O. Aremu, C.J. Tuck, I.A. Ashcroft, Compressive failure modes and energy absorption in additively manufactured double gyroid lattices, Addit. Manuf. 16 (2017) 24–29.

[58] S. Bargmann, B. Klusemann, J. Markmann, J.E. Schnabel, K. Schneider, C. Soyarslan, J. Wilmers, Generation of 3D representative volume elements for heterogeneous materials: a review, Prog. Mater. Sci. 96 (2018) 322–384.

[59] A. Gautam, R.K. Yadav, K.P. Ajit, V.K. Rajak, A review on CDM-based ductile models and its application, Trans. Indian Inst. Met. 76 (5) (2023) 1141–1154.

[60] M. McGregor, S. Patel, S. McLachlin, M. Vlasea, Architectural bone parameters and the relationship to titanium lattice design for powder bed fusion additive manufacturing, Addit. Manuf. 47 (2021) 18.

[61] C.X. Wang, J.E. Liu, S.Y. Min, Y. Liu, B.C. Liu, Y.Y. Hu, Z.G. Wang, F.B. Mao, C. M. Wang, X.L. Ma, P. Wen, Y.F. Zheng, Y. Tian, The effect of pore size on the mechanical properties, biodegradation and osteogenic effects of additively manufactured magnesium scaffolds after high temperature oxidation: an *in vitro* and *in vivo*, Bioact. Mater. 28 (2023) 537–548.

[62] D. Schönegg, A. Koch, G.T. Müller, M. Blumer, M.E.H. Wagner, Two-screw osteosynthesis of the mandibular condylar head with different screw materials: a finite element analysis. Computer Methods in Biomechanics and Biomedical Engineering, 2023.

[63] J.H. Oh, Y.S. Kim, J.Y. Lim, B.H. Choi, Stress distribution on the prosthetic screws in the all-on-4 concept: a three-dimensional finite element analysis, J. Oral Implantol. 46 (1) (2020) 3–12.

[64] Y. Hirai, K. Watanabe, T. Deguchi, K. Ueda, K. Hamada, E. Tanaka, Influence of insertion depth on stress distribution in orthodontic miniscrew and the surrounding bone by finite element analysis, Dent. Mater. J. 40 (5) (2021) 1270–1276.

[65] C.M. Haslauer, J.C. Springer, O.L.A. Harrysson, E.G. Loboa, N.A. Monteiro-Riviere, D.J. Marcellin-Little, *In vitro* biocompatibility of titanium alloy discs made using direct metal fabrication, Med. Eng. Phys. 32 (6) (2010) 645–652.

[66] F. Bartolomeu, M.M. Costa, N. Alves, G. Miranda, F.S. Silva, Selective Laser Melting of Ti6Al4V sub-millimetric cellular structures: prediction of dimensional deviations and mechanical performance, J. Mech. Behav. Biomed. Mater. 113 (2021) 9.

[67] J.P. Li, J.R. de Wijn, C.A. van Blitterswijk, K. de Groot, The effect of scaffold architecture on properties of direct 3D fiber deposition of porous Ti6Al4V for orthopedic implants, J. Biomed. Mater. Res., Part A 92A (1) (2010) 33–42.

[68] J.J. Weng, Y. Su, Nuclear matrix-targeting of the osteogenic factor Runx2 is essential for its recognition and activation of the alkaline phosphatase gene, Biochim. Biophys. Acta Gen. Subj. 1830 (3) (2013) 2839–2852.

[69] P. Ducy, R. Zhang, V. Geoffroy, A.L. Ridall, G. Karsenty, Osf2/Cbfa1: a transcriptional activator of osteoblast differentiation, Cell 89 (5) (1997) 747–754.

[70] U. Kresnoadi, M. Nizar, Soekobagiono, increased expression of RUNX2 and ALP resulting from a combination of propolis extract and bovine bone graft in socket preservation material, Braz. J. Pharm. Sci. 58 (2022) 12.

[71] S. Thanakun, C.P.N. Mahasarakham, S. Pomprasertsuk-Damrongsri, Y. Izumi, Correlation of plasma osteopontin and osteocalcin with lower renal function in dental patients with carotid artery calcification and tooth loss, J. Oral Biosci. 61 (3) (2019) 183–189.

[72] J.Y. Si, C.W. Wang, D.H. Zhang, B. Wang, W.W. Hou, Y. Zhou, Osteopontin in bone metabolism and bone diseases, Med. Sci. Mon. Int. Med. J. Exp. Clin. Res. 26 (2020) 9.

[73] A. Singh, G. Gill, H. Kaur, M. Amhmed, H. Jakhu, Role of osteopontin in bone remodeling and orthodontic tooth movement: a review, Prog. Orthod. 19 (2018) 8.

[74] M. Ikegame, S. Ejiri, H. Okamura, Expression of non-collagenous bone matrix proteins in osteoblasts stimulated by mechanical stretching in the cranial suture of neonatal mice, J. Histochem. Cytochem. 67 (2) (2019) 107–116.

[75] T. Komori, Functions of osteocalcin in bone, pancreas, testis, and muscle, Int. J. Mol. Sci. 21 (20) (2020) 15.

[76] E. Duman, E.S. Kehribar, R.E. Ahan, E. Yuca, U. Seker, Biomineralization of calcium phosphate crystals controlled by protein-protein interactions, ACS Biomater. Sci. Eng. 5 (9) (2019) 4750–4763.

[77] J.J. Luo, M. Tamaddon, C.Y. Yan, S.H. Ma, X.L. Wang, F. Zhou, C.Z. Liu, Improving the fretting biocorrosion of Ti_6Al_4V alloy bone screw by decorating structure optimised TiO_2 nanotubes layer, J. Mater. Sci. Technol. 49 (2020) 47–55.

[78] H. Liang, T. Ji, Y. Zhang, Y. Wang, W. Guo, Reconstruction with 3D-printed pelvic endoprostheses after resection of a pelvic tumour, Bone Joint Lett. J 99B (2) (2017) 267–275.

[79] R. Jayasree, K. Raghava, M. Sadhasivam, P.V.V. Srinivas, R. Vijay, K.G. Pradeep, T. Rao, D. Chakravarty, Bi-layered metal-ceramic component for dental implants by spark plasma sintering, Mater. Lett. 344 (2023) 4.

[80] J.H. Tan, C.K. Cheong, H.W.D. Hey, Titanium (Ti) cages may be superior to polyetheretherketone (PEEK) cages in lumbar interbody fusion: a systematic review and meta-analysis of clinical and radiological outcomes of spinal interbody fusions using Ti versus PEEK cages, Eur. Spine J. 30 (5) (2021) 1285–1295.

[81] A. Ronca, L. Ambrosio, D.W. Grijpma, Design of porous three-dimensional PDLLA/nano-hap composite scaffolds using stereolithography, J. Appl. Biomater. Funct. Mater. 10 (3) (2012) 249–258.